Realistic Model to Predict the Macrostructure of GTAW Welds for the Simulation of Ultrasonic Non destructive Testing

Quentin Marsac, Cécile Gueudré, Marie-Aude Ploix, Laurent Forest, François Baqué, Gilles Corneloup

Title

Realistic model to predict the macrostructure of GTAW welds for the simulation of ultrasonic non destructive testing

Authors' names and affiliations
Quentin MARSAC[1,2,*], Cécile GUEUDRE[2], Marie-Aude PLOIX[2], Laurent FOREST[3], François BAQUÉ[1], Gilles CORNELOUP[2]

[1] CEA-DES-IRESNE-DTN-STCP-LISM Cadarache F-13108 Saint-Paul-Lez-Durance, France
[2] Aix Marseille Univ, CNRS, Centrale Marseille, LMA UMR 7031, Marseille, France
[3] DES-Service d'études mécaniques et thermiques (SEMT), CEA, Université Paris-Saclay, F-91191 Gif sur Yvette, France

[*]Corresponding author
Phone number: +33 (0) 4 42 93 90 34
E-mail address: quentin.marsac@cea.fr
Postal Address: Laboratoire de Mécanique et d'Acoustique, CNRS - UMR 7031
Aix Marseille Université, IUT GMP
413 Avenue Gaston Berger
13 625 Aix en Provence Cedex1, France

Abstract

The knowledge of grain growth directions makes it possible to describe the material anisotropy, which helps to ensure the ultrasonic testing of welded assemblies and the assessment of their mechanical integrity. Here, we study multipass welds made of 316 L stainless steel manufactured by a Gas Tungsten Arc Welding (GTAW) process. We have developed a specific model to predict the grain growth directions using a phenomenological solidification model relevant for GTAW welds. This new model follows the philosophy of the MINA model, developed since 2000 and which predicts the grain growth directions for Shielded Metal Arc Welding (SMAW) multipass welds, taking into account information from the welding notebook and macrograph analysis. Unlike the MINA model, the new model does not require measurement of the remelting parameters on macrographs, which can be complex to perform. These parameters are calculated from the measurement of dimensions on associated beads on plate. In this paper, the development of this new model is presented and the results are shown.

Keywords: stainless steel multipass weld, GTAW, macrostructure modelling, grain growth, ultrasound, NDT.

1. Introduction

The primary circuit in Sodium Fast Reactors includes numerous structures and components, such as the main vessel, primary pumps, heat exchangers, containing high temperature sodium. They are made of austenitic stainless steel, as it exhibits excellent corrosion resistance and very good mechanical strength at high temperature. Non-destructive examination aims to detect potential defects in the numerous welds that could be present in the primary circuit and at characterizing these defects (position and dimensions), so that their severity can be assessed. This non-destructive testing can be performed by the ultrasonic method. However, the ultrasonic testing of thick multipass austenitic stainless steel welds is complex because the macrostructure of these welds is both anisotropic (grain elongation parallel to the lines of heat dissipation with preferential crystallographic direction <100> [1]) and heterogeneous (variation of grain orientation in the welded volume), see example in Figure 1.a. Consequently, the propagation of the ultrasonic beam is altered due to the phenomena of deviation and splitting of the ultrasonic beam (Figure 1.b), as well as attenuation and structure noise [2,3] distorting the signal interpretation and diagnosis.

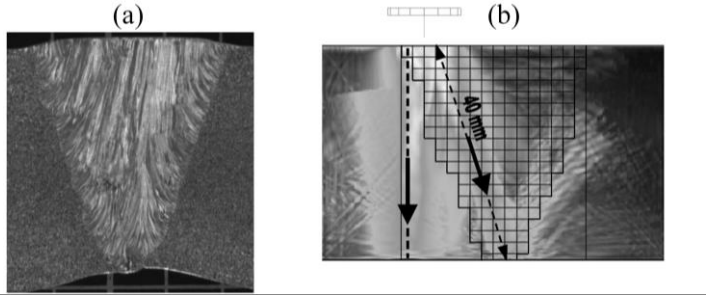

Figure 1: (a) Macrograph of SMAW weld ; (b) Ultrasonic propagation simulated with the ATHENA code: deviation and splitting of the ultrasonic beam. Extracted from [4].

Therefore, in order to make the signal interpretation and diagnosis reliable, the effects on the ultrasonic beam should be predicted, whatever the welding process. That prediction can be performed with a numerical modelling that involves the knowledge of the macrostructure of the weld and a code simulating the ultrasonic propagation.

Numerous ultrasonic propagation simulation codes are used in the literature to address the problem of ultrasonic testing of polycrystalline metals with both anisotropic and heterogeneous structures. Many of them are based on ray-tracing methods [5–8] such as CIVA software which use a Dynamic Ray Tracing (DRT) method to evaluate the trajectory, the time of flight of the rays, and the amplitude associated with a ray tube during propagation [9,10]. DRT is applied on a smooth representation of the elastic properties of the weld [11] and model the beam to flaw interaction [12]. The ATHENA code used for this study and developed by EDF (Électricité De France) and INRIA (Institut National de Recherche en Informatique et Automatique) is a finite element code that solves the elastodynamic equations, in the transient regime, in a heterogeneous and anisotropic medium [13,14]. The weld is described in the ATHENA code by a finite number of homogeneous orthotropic domains (meshes), each domain being defined by a local grain orientation. Based on the set of elasticity constants of the welded metal, local elasticity constants are then deduced from those orientations.

The simulation requires a realistic description of the weld as input data: geometry, material and macrostructure. Some models at the macroscopic scale exist, most of them considering a symmetrical description [5,15–17]. The Ogilvy's model [5] is the most commonly used. The realistic MINA model [4] developed by LMA (Laboratoire de Mécanique et d'Acoustique), EDF and Naval Group, is based on the phenomenology of the SMAW (Shielded Metal Arc Welding) process. All of these models describe the macrostructure in the weld cross-section (2D models), which has been demonstrated to be sufficient in the case of downhand position welds [18]. We therefore maintain this assumption.

The welds studied here were manufactured using the Gas Tungsten Arc Welding (GTAW) process, with Arc Voltage Control (AVC) and robotized axes, in downhand position. The ability of two models (Ogilvy and MINA) was tested on GTAW welds, and this has shown significant errors, due to the symmetrical hypothesis of the Ogilvy model, and due to the difference of the welding parameters between SMAW process and GTAW process for the MINA model. Consequently, this test highlight the need to develop a new phenomenological model, relevant for the GTAW process. Hence, we decided to rely on MINA main lines while adopting a new approach for calculating phenomenological parameters based on the analysis

and measurement of dimensions of corresponding beads on plate. The advantage is that the beads on plate are generally available because manufactured for each weld in order to adjust the welding parameters.
Section 2 presents the GTAW welding parameters used here. Section 3 develops the grain growth direction prediction model, first by presenting the phenomenological parameters, then the calculation of the directions of the thermal gradient within a bead and the impact of the position of the pass in the chamfer on the directions of the thermal gradient. Finally, the principle of calculating grain growth directions is explained. Section 4 discusses the results and the relevance of the model, by comparing the macrostructures predicted by the model with those measured on the macrographs of the GTAW weld mock-ups performed, and then comparing the results of ultrasonic simulations.

2. Definition of mock-ups and beads on plate

We designed and manufactured various thick multipass GTAW welding mock-ups to analyse their macrostructures. The welding parameters that we chose to vary are those that mainly vary in the case of industrial welds, and that potentially influence the macrostructure of the weld, i.e., arc voltage (U), intensity (I) and welding speed (S). Table 1 shows the values of these parameters for the four mock-ups, chosen from usual values and tests on beads on plate in order to guarantee the welds are without defects such as lack of fusion, porosity, etc.

Reference mock-ups	Arc voltage U (V)	Intensity I (A)	Welding speed S (mm/min)	Power $P = U * I$ (W)	Heat input $E = (U * I)/S$ (kJ/cm)
E1UI	10	190	164	1900	6.95
E2UI	12	290	164	3480	12.7
E1S	12	290	300	3480	6.95
E3S	12	290	105	3480	19.9

Table 1: Value of the welding parameters associated with the 4 GTAW mock-ups.

In order to maintain the same operating conditions for all passes, there is no root pass. The welds studied are made on 25 mm thick plates, grooved, with a ligament thickness of 5 mm. The geometry of the chamfer is V-shaped, 20 mm high, 31 mm wide at the top and 3 mm wide at the bottom. Furthermore, the maximum inter-pass temperature is fixed at 150°C in order to minimize the risk of hot cracking.
On the one hand, the E1UI and E2UI mock-ups make it possible to study the influence of the welding power on the macrostructure: the welding speeds are identical while the arc voltage and intensity are different. On the other hand, the E1S and E3S mock-ups are manufactured with the same welding power as E2UI but with different welding speeds, therefore different heat inputs. Thus, the E2UI, E1S and E3S mock-ups will make it possible to analyse the influence of the heat input on the macrostructure for the same welding power.

Other welding parameters could influence the macrostructure, such as: the type of the shielding gas [19,20], the sulphur content of base and filler metals [21–24], the tip angle of electrode [25,26] as well as the welding position [18,27]. We chose to set these parameters: base metal (316L) and filler metal (Z4 Cr Ni Mo 17-11-2) with sulphur content below 50 ppm, wire feed rate (2000 mm/min, cold wire), wire diameter (0.9 mm) - and therefore the deposition rate (product of the density of the wire by the wire feed rate and the wire cross-section) is fixed at 0.61 kg/h - , electrode diameter and tip angle (3.2 mm and 60°, respectively), type of the shielding gas (100% Argon) and welding position (downhand).

Previous studies on the SMAW process have shown that the order of the passes is very influential on the grain growth directions [28,29]. In the case of our study, the order of the passes is defined and fixed for all the mock-ups, in the left-right AMerican style (Figure 2, for each layer, the passes are alternately placed at the ends of the chamfer until they reach the centre of the weld). This is integrated into our model but fixed for the moment.

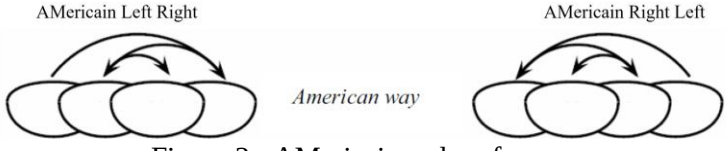

Figure 2 : AMericain order of passes.

3. Model to predict the grain growth directions

The grain growth direction prediction model is based on the study of the effects of welding parameters on beads on plate (single pass) as well as on multipass weld mock-ups. This model uses as input data the information from the welding notebook (chamfer dimensions, number of layers, number of passes per layer, sequence of passes and welding parameters), as well as four phenomenological parameters (see diagram in Figure 3) : the pass width W_{Pass}, the vertical remelting R_v, the total pass height H_{Pass} and the lateral remelting R_l. The model calculates the directions of the thermal gradient within a single pass, then takes into account the position of the pass in the chamfer. Since the maximum inter-pass temperature is fixed at 150°C, its effect on the thermal gradient is negligible.. It then reproduces the two solidification mechanisms within a multipass weld: epitaxial growth - a grain in formation adopts the direction of the grains on which it rests, leading to the formation of columnar grains [26] - and selective growth - when two grains "cross", the grain that will continue to grow is the one whose growth direction (i.e., crystallographic direction <100>) is the closest to the local direction of the thermal gradient [30].

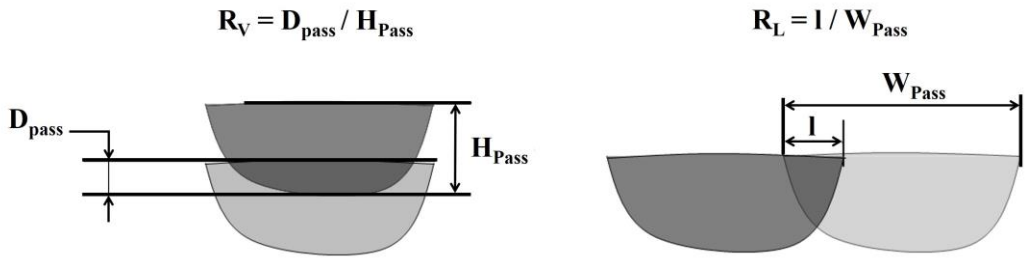

Figure 3: Phenomenological parameters: vertical remelting (R_v) and lateral (R_l), as well as pass dimensions (width W_{Pass} and height H_{Pass}).

3.1. Phenomenological parameters: measurements and calculations on beads on plate

Among the four phenomenological input parameters of the model, we chose to measure one (the pass width W_{Pass}), directly on the beads on plate and the other three (vertical remelting R_v, total pass height H_{Pass} and lateral remelting R_l) are calculated from the measurements made on the beads on plate (bead width W_{Bead}, penetration depth D_{Bead}, and reinforcement height R_{Bead}). This is the main advance over the MINA model, for which these parameters are measured on representative weld macrographs [4]. The choice was made to integrate only the W_{Pass} direct measurement into the model, because the comparison between the bead on plate and the weld pass proved to be good for the width W_{Pass}, but not for the height H_{Pass}.
Table 2 presents the values of the welding parameters of the beads on plate manufactured and studied (the other parameters fixed are identical to those of the mock-ups). A total of 15 beads on plate were manufactured in order to analyse dimensional variations according to welding parameters and possibly to derive trends or laws.

N° beads on plate	U (V)	I (A)	S (mm/min)	$P = U * I$ (W)	$E = (U * I)/S$ (kJ/cm)
Beads 1 to 5	10	190	75-125-164-200-250	1900	4.5-15.2
Bead 6	11	190	164	2090	7.6
Bead 7	11	240	164	2640	9.6
Bead 8	11	290	164	3190	11.6
Beads 9 to 15	12	290	75-105-125-164-200-250-300	3480	6.95-27.9

Table 2: Welding parameters of the beads on plate (total 15), classified into 5 levels of welding power.

Figure 4 illustrates the three characteristic dimensions that are measured on each of the beads on plate: reinforcement height (R_{Bead}), depth of penetration (D_{Bead}) and width (W_{Bead}). And we note the total height of the bead on plate $H_{Bead} = R_{Bead} + D_{Bead}$.

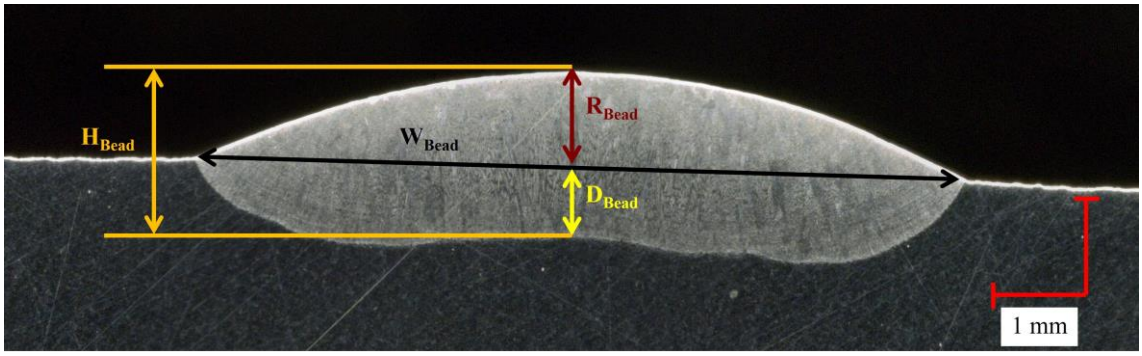

Figure 4: Characteristic dimensions of a bead on plate.

The evolution of these characteristic dimensions with the welding speed S is plotted in Figure 5. Some points are worth noting when considering these measures. First of all, from a general point of view, the three dimensions evolve in a manner that is inversely proportional to the welding speed. These observations are in accordance with the data in the literature [23].

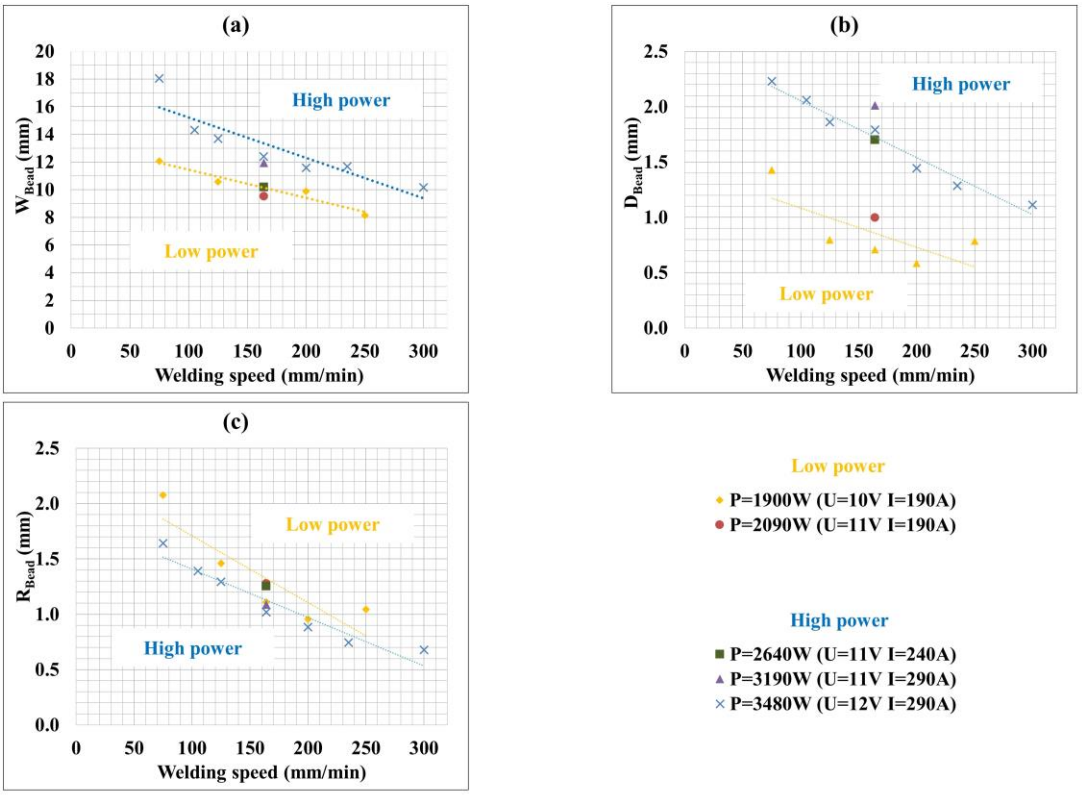

Figure 5: Evolution of the characteristic dimensions measured for 5 welding powers as a function of the welding speed: (a) bead width, (b) bead penetration depth, (c) bead reinforcement height.

Whatever the welding speed, bead width W_{Bead} (Figure 5.a) and bead penetration depth D_{Bead} (Figure 5.b) measured for low powers (in yellow) are always lower than those for high powers (in blue), while the opposite holds true for the bead reinforcement height R_{Bead} (Figure 5.c). Indeed, between two beads laid at the same welding speed (and therefore with the same volume), a decrease in power and therefore in width implies an increase in bead reinforcement height.

Over the ranges of welding parameter values studied, power has a significantly greater effect on the penetration and bead width than on the height of the curved bead. The evolution of the dimensions W_{Bead}, D_{Bead} and R_{Bead} of a bead on plate within these ranges of parameter values can be approximated by a linear regression law in each power group.

We now compare the width W_{Bead} from beads on plate with pass widths W_{Pass} measured on the mock-ups to validate its use in the model. We choose to measure the width pass only on the last layer passes (at the top of the weld, see example in Figure 6) because these passes are not affected by the vertical re-melting. Therefore, it facilitates the estimation of the pass contour. And it seems reasonable to postulate that the widths are similar in the full thickness of the weld (excepted for the very first layers, see below). The measurements of W_{Pass} are performed on the macrographs of the four mock-ups (E1UI, E2UI, E1S and E3S), where the number of passes involved is 6, 5, 15 and 3, respectively.

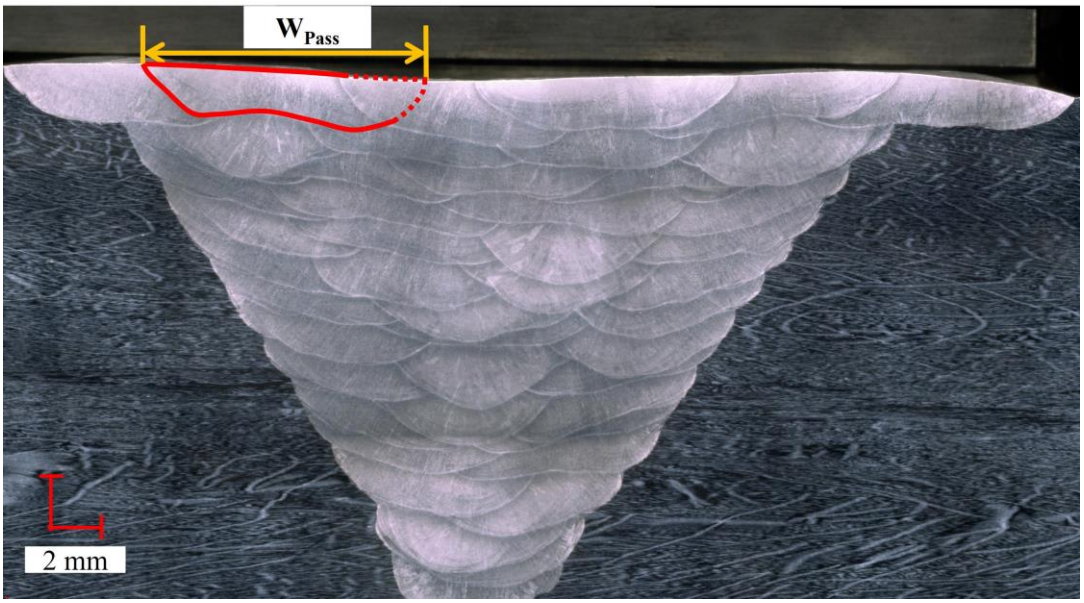

Figure 6: Macrograph of E1UI weld where the number of passes of the last layer is 6. Measurement of the pass width (W_{Pass}) after contour plotting (in red), extrapolated for laterally remelted parts (red dotted lines).

Table 3 presents the comparison of the average pass widths (Mean W_{Pass}) measured on the mock-ups, with the corresponding bead on plate widths (W_{Bead}), measured on the beads on plate. It is clearly observed that the measurements on the beads on plate are in very good agreement with those on the mock-ups at the last layer, with maximum deviations of less than 10%. Thus, estimating the pass width of the last layer from the measurements on the beads on plate is a valid approach.

Reference	Mean W_{Pass} (mm)	W_{Bead} (mm)	Discrepancy
E1UI	10.6	10.2	4%
E2UI	13.3	12.3	8%
E1S	11.1	10.2	9%
E3S	15.6	14.3	9%

Table 3: Comparison of the average pass widths measured on the mock-ups with the bead widths measured on the beads on plate.

However, we observed on the macrographs (see example Figure 6) that the pass width is smaller at the first layers than in the rest of the weld. In fact, the chamfer width at the first layers is smaller than the width of the passes. Consequently, we chose to adapt for those cases the pass widths according to the width of the chamfer.

The measurement of the vertical remelting parameters (R_v) on weld macrographs requires the estimation of the pass contour. Thus, we chose to calculate the value of this parameter from the measurements from the beads on plate:

$$R_v = \frac{D_{Bead}}{H_{Bead}} \quad (1)$$

The results reported in Figure 7 show that this parameter, under the previously established fixed conditions (in particular deposition rate), does not depend on the welding speed, but only on the welding power. The two power groups are again distinguished: for low powers, the average value of R_v is 0.39 (orange line) and for high powers, 0.61 (blue line). Thus, we conclude that a variation in welding power of about 10% (variation in power within each group) has little influence on the value of the vertical remelting parameter. These power variations within each group are of the same order as those encountered in the industrial case (arc voltage at ± 1V and intensity at ± 10A). We therefore assume that the prediction of the vertical remelting parameter from the average data from the welding notebook is satisfactory.

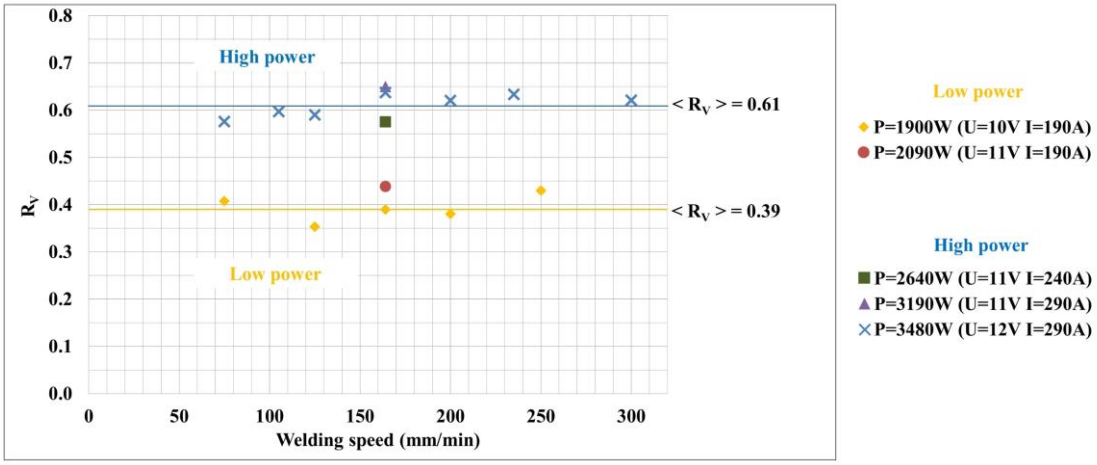

Figure 7: Evolution of the vertical remelting parameter for 5 welding power levels as a function of the welding speed.

The total pass height H_{pass} is calculated from data from the welding notebook (height h of the chamfer, number of layers N_L) and the vertical remelting parameter:

$$H_{pass} = \frac{h}{N_L * (1 - R_v)} \quad (2)$$

As for the lateral remelting parameter, R_l cannot be calculated directly from the measurements of the dimensions on the beads on plate, because physically it depends on the layer width, the number of passes per layer and the width of each pass. Thus, by assuming that R_l is constant within the same layer and can vary from one layer to another, we calculate for each layer k the value of the lateral remelting parameter $R_l(k)$ by first determining the vertical position $G_y(k)$ of the layer k in the chamfer, then its width $W_{layer}(k)$ from the dimensions of the chamfer and the vertical remelting:

$$G_y(k) = H_{Pass} * (1 - R_v) * k \quad (3)$$

$$W_{layer}(k) = b + \frac{\frac{1}{2} * (c - b)}{h} * G_y(k) * 2 \quad (4)$$

where b is the width at the bottom of the chamfer, c is the width at the top and h is the height. Finally $R_l(k)$ is calculated as follows:

$$R_l(k) = 1 - \frac{W_{layer}(k) - W_{Pass}}{(N_{Pass}(k) - 1) * W_{Pass}} \quad (5)$$

where $N_{Pass}(k)$ is the number of passes in the k layer.

3.2. Calculation of the thermal gradient in a pass

As the grain growth is directly related to the thermal gradient, we start by analysing a bead on plate in order to develop the calculation of the thermal gradient in an isolated pass, α_g^{init}, then for a pass in the chamfer with consideration of the surrounding metal, α_g.

Figure 8 shows that the grain growth directions (yellow and black arrows) are generally symmetrical with respect to the axis of the bead on plate (dotted white line), and that three zones can be distinguished: the central zone (orange) with rectangular geometry and the lateral zones (blue) with square geometry. The lateral zones are characterized by varying grain growth directions, while the central zone is characterized by grain growth directions rather parallel to each other and to the axis of symmetry of the weld.

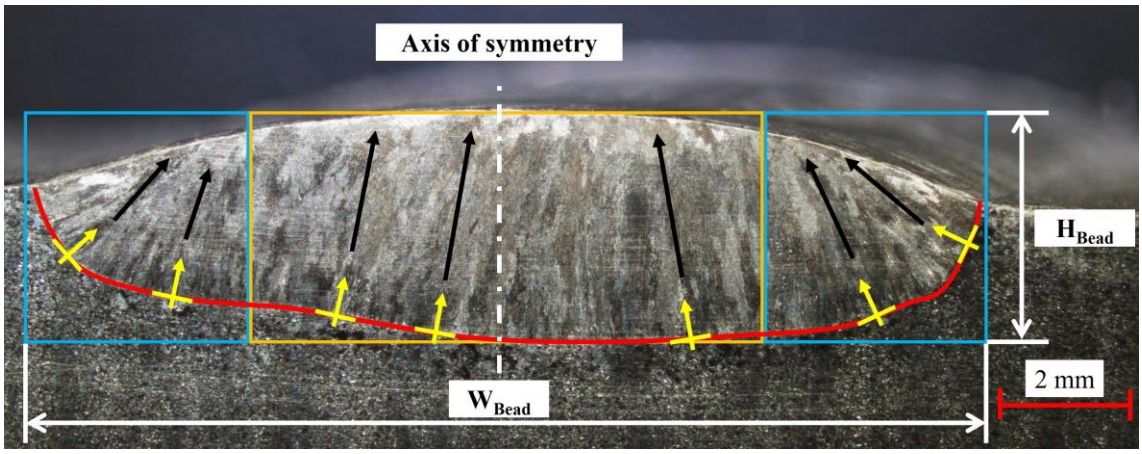

Figure 8 : Analysis of the macrostructure of the beads on plate: definition of 3 grain growth zones.

Figure 8 also shows that the grain growth at the contour is orthogonal to this contour (yellow arrows). However, the latter corresponds to an isotherm (solidus) and by definition the thermal gradient is orthogonal to the isotherms. Therefore, we assume that the directions of the thermal gradient are orthogonal to this contour. Figure 8 highlights that the grains within the bead are straight (black arrows), and so we assume that the thermal gradient is also straight. The grains do not cross within the pass, and so selective growth within the pass alone is very limited. In order to reproduce these different observations and automatically calculate the directions of the thermal gradient, we consider here the contour of a pass with a "U-flat" shape (Figure 9). The ends of the pass are quadrants of a circle whose radius is the total height of the pass. Thermal gradient directions α_g^{init} are then calculated to be normal to the modelled contours.

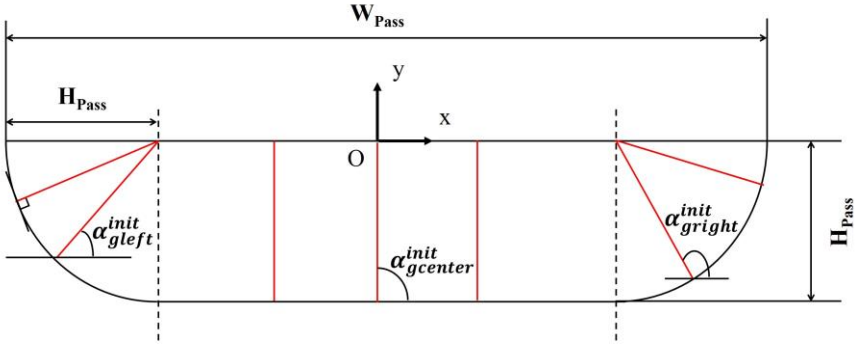

Figure 9: Illustration of the directions of the thermal gradient ($\alpha_{gleft}^{init}, \alpha_{gcenter}^{init}, \alpha_{gright}^{init}$) calculated for each area of the bead.

The initial thermal gradient α_g^{init} in a single pass being modelled, it must now be adapted to take into account the fact that the pass is deposited at a certain position in the chamfer. Indeed, the position of the pass in the chamfer has an impact on the average orientation of the grains in the pass. Figure 10 shows the average grain orientation for three passes in the chamfer. As for those with a yellow outline, one is located at the edge of the chamfer and the other within the weld that rests laterally on a single pass. For these passes, the average grain orientation is strongly inclined, which means an overall inclination of the thermal gradient directions. The green contour pass corresponding to a last pass in a layer (resting laterally on two passes), the average grain orientation is vertical.

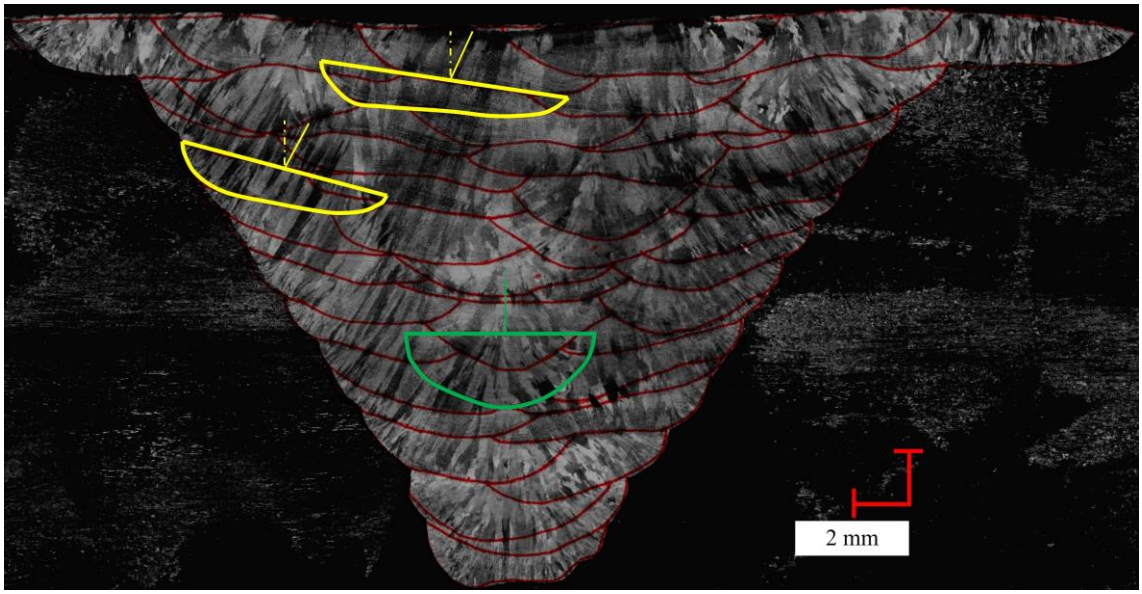

Figure 10: Example of E1UI. Influence of the position of the pass in the chamfer: last pass in a layer (green contour) and pass at the edge or within the weld resting on a single pass (yellow contour).

These observations can be explained, by a symmetrical balance of heat flow for the last passes per layer because the quantities of heat transmitted (by thermal conduction) from the pass to the surrounding material are then almost symmetrical. On the other hand, for the other passes, there is an asymmetrical balance of the heat flows transmitted to the surrounding metal.

Fourier's law shows the direct link between the directions of heat flow and the directions of the thermal gradient:

$$\vec{q} = -\lambda . \overrightarrow{grad}(T) \tag{6}$$

where $\vec{q}$ represents the surface density of the heat flux ($W.m^{-2}$), λ represents the thermal conductivity of the medium ($W.m^{-1}.K^{-1}$) and $\overrightarrow{grad}(T)$ represents the thermal gradient ($K.m^{-1}$).

The initial directions of the thermal gradient calculated above are therefore modified by a value β for all passes except for the last ones per layer, β resulting from the calculation of the asymmetrical balance of heat flows on the contours of the pass:

$$\alpha_g = \alpha_g^{init} \pm \beta \tag{7}$$

where the sign (-) is associated with the passes on the left and the sign (+) with the passes on the right, and

$$\beta = \tan^{-1}\left(\frac{H_{Pass}.(1-R_{VPass}).\left(1+\frac{H_{Pass}}{H_{Pass}+W_{Pass}}\right)}{W_{Pass}+H_{Pass}.(1-R_{VPass}).\left(\frac{W_{Pass}}{H_{Pass}+W_{Pass}}\right)}\right) \tag{8}$$

3.3. Calculation of grain growth directions: solidification mechanisms

The calculation of thermal gradient directions α_g was established from analyses on beads on plate and mock-ups to take into account the effect of the position of the pass on the directions of the thermal gradient. The principle of the model is to build the weld pass by pass, taking into account the order of the passes, the welding notebook, and therefore to take into account the passes previously deposited. For the first layers, the pass widths are adapted according to the width of the chamfer.

To integrate the complexity of the solidification mechanisms into the model, a grain growth calculation was developed. This calculation was performed locally, in a mesh size of 0.5×0.5 mm². Indeed, macrographic analyses had confirmed that a mesh size of 0.5×0.5 mm² allows the physics of the problem to be well represented at the grain scale [4]. A pass is modelled with a rectangular geometry and meshed as shown on Figure 11. Thus for each mesh (i, j) of the pass (i being the line number and j the column number), the direction of the thermal gradient is $\alpha_g(i, j)$. The grain growth direction in (i, j) is noted $\theta(i, j)$.

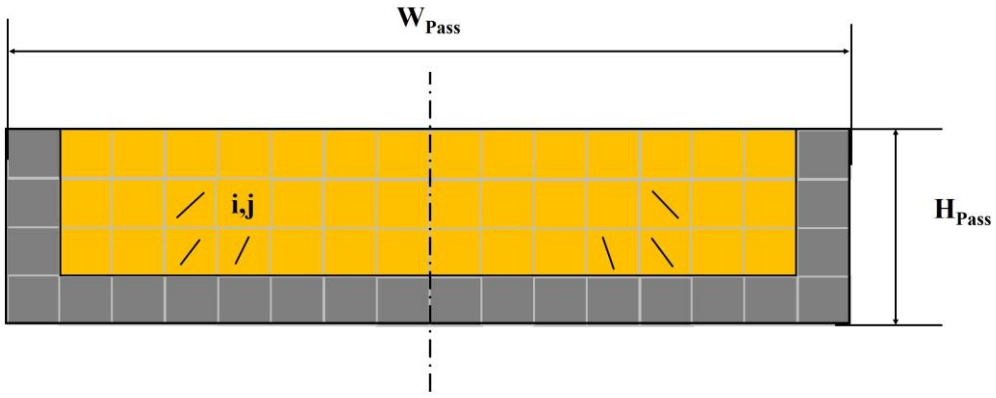

Figure 11: Example of modelling of a rectangular geometry pass with dimensions of 8×2 mm²: calculation of grain growth directions on the contour of the pass (grey mesh) and within the pass (orange mesh).

3.3.1. On the contour of the pass

For the meshes next to the chamfer, the grain directions are simply defined equal to those of the thermal gradient: $\theta(i, j) = \alpha_g(i, j)$.

Concerning the remelting of a pass on one or more than one other pass, selective growth can come into play. Indeed, macrographs show in places sudden variations in grain growth directions, when remelting a pass on another pass. The minimum difference in measured direction variation is about 40° (Figure 12, yellow arrows). We therefore assume that the selective growth mechanism dominates when the absolute difference in angle between the thermal gradient and the grain growth direction is greater than 40°.

The directions of the grains on the contour of a pass deposited on (or against) another pass are therefore defined equal to those of the grains on which they rest (epitaxial growth): $\theta(i, j) = \theta(i, j - 1)$ on the left, or $\theta(i, j) = \theta(i - 1, j)$ at the bottom, unless the absolute difference between these directions ($\theta(i - 1, j)$ or $\theta(i, j - 1)$) and $\alpha_g(i, j)$ is greater than 40°. In this case, the grain directions are defined equal to those of the thermal gradient: $\theta(i, j) = \alpha_g(i, j)$.

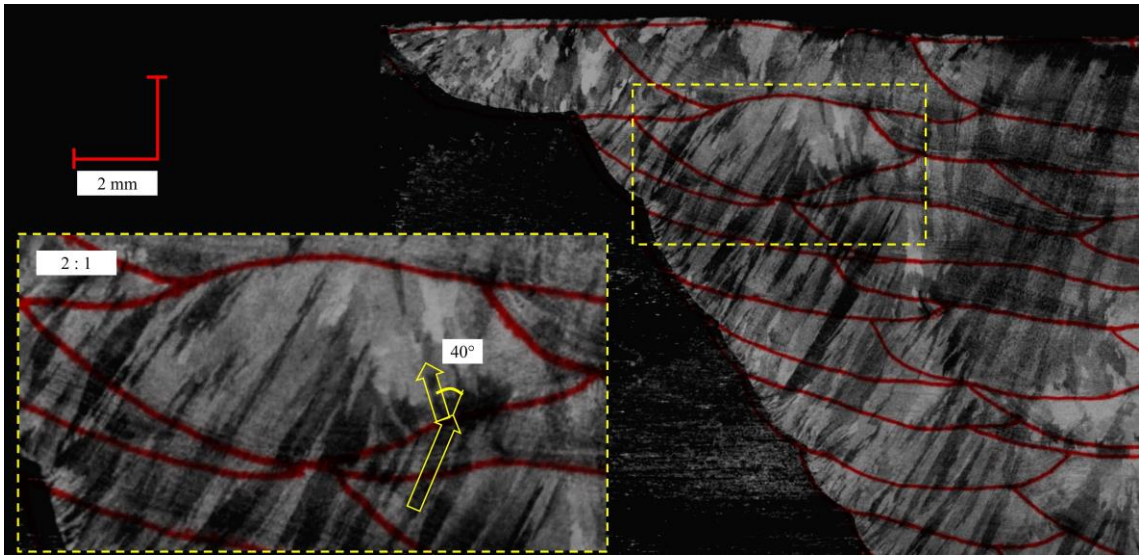

Figure 12: Selective growth (yellow arrows): sudden change in growth direction.

3.3.2. Within the pass

The direction of a grain in the mesh (i,j) within the pass depends on the directions in the adjacent meshes, the thermal gradient, and the possible epitaxy.

It should be noted that $\bar{\theta}(i,j)$, the average direction around the mesh (i,j), is calculated for the left part of the pass by:

$$\bar{\theta}(i,j) = \frac{\theta(i,j-1) + \theta(i-1,j-1) + \theta(i-1,j)}{3} \quad (9)$$

and $e(i,j)$ is the absolute difference in direction between the average grain $\bar{\theta}(i,j)$ and the thermal gradient $\alpha_g(i,j)$:

$$e(i,j) = \left|\bar{\theta}(i,j) - \alpha_g(i,j)\right| \quad (10)$$

If $e(i,j)$ is less than 40°, then the growth occurs through the epitaxy mechanism, and:

$$\theta(i,j) = \cos\big(e(i,j)\big).\bar{\theta}(i,j) + \big[1 - \cos\big(e(i,j)\big)\big].\alpha_g(i,j) \quad (11)$$

However, if $e(i,j)$ is greater than 40°, then the growth is selective, and we have:

$$\theta(i,j) = \alpha_g(i,j) \quad (12)$$

4. Results and discussion

The relevance of the model is assessed in two ways: first by comparing the grain growth directions measured on the macrographs with those predicted by the model, and then by comparing the ultrasonic results (maxima of ultrasonic amplitudes after propagation through the weld) simulated using the ATHENA finite element code, through the macrostructure (grain growth directions) measured on macrographs and the macrostructure predicted by the model.

4.1. Comparison between modelled and measured macrostructures

As mentioned above, the grain directions were measured on the macrographs of the four mock-ups in a mesh size of 0.5×0.5 mm². Two types of average errors (in degrees) between the directions measured on the macrograph and predicted by the model were calculated. We first calculated the global average error $\Delta\theta_G$ (average of the absolute errors of all meshes), and the standard deviation σ_G of this error in order to analyse its dispersion. This global error represents both the gaps within the welded area and also at the edges (i.e. the chamfer). In the latter case, the difference can be significant, mainly due to three sources of error: the modelled pass shape, which is rectangular whereas the actual pass shape is more of the "U-flat" type, the failure to take into account the dilution at the edges of the chamfer by the model and the failure to take into account the geometric inclination of the passes by the model (only the thermal inclination is adopted). This results in meshes identified simultaneously as welded metal in the model and base metal on the macrograph, and conversely. For this purpose, the error $\Delta\theta_W$ within the welded zone and its associated standard deviation σ_W were also calculated. In this case, only the deviations of orientation in the meshes where the model and the measurement both concern welded metal were retained. Figure 13 maps the local errors and gives the associated values of average errors, with their respective standard deviations.

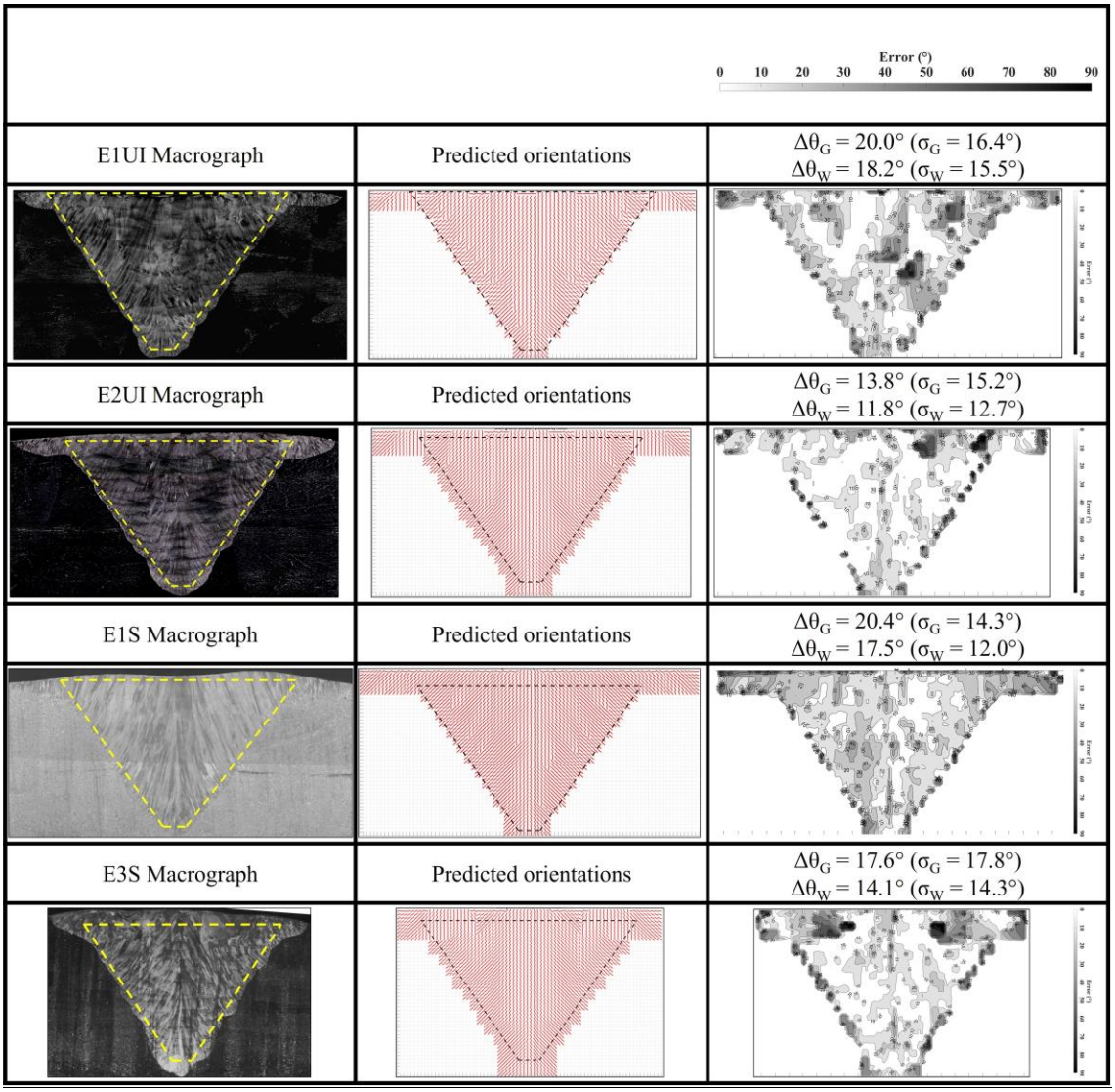

Figure 13: Comparison of grain directions measured on macrographs and predicted by the model for the 4 welding mock-ups.

Modelling errors within the welded areas are relatively small, the white areas correspond to deviations of less than 10°. Thus, the model is in good agreement with the actual macrostructures.
For the four mock-ups, the global average error is between 14° and 20°. The maps of the local errors show that the errors are rather localized for the E1UI, E2UI and E3S mock-ups (the value of the associated standard deviation is relatively high: between 15.3° and 17.8°). Indeed, for the E2UI and E3S mock-ups, these errors are located at the last welding layer where the passes have a parabolic shape, and not a shape of the "U-flat" type (leading to a different thermal gradient). For E1UI mock-up, these errors are located within the welded area, at the location of two passes identified on macrograph, which are particularly inclined while the others are rather horizontal. This local inclination is not really explained, and is not taken into account in the model.

Conversely, the map of the local errors for E1S welding shows that the errors observed are rather distributed over the whole weld (the value of the associated standard deviation is lower, equal to 14.3°). Indeed, the welding speed for this mock-up is very important (300 mm/min), which seems to have an impact on the directions of the thermal gradient and therefore on the grains [23]. We are at the limit of the model's validity here.

4.2. Comparison of simulated ultrasonic results

The objective of the model is not to perfectly represent the macrostructure of a weld but to predict the propagation of the ultrasonic beam through the weld. Thus, we compared the simulated ultrasonic results through the measured and predicted grain directions using the ATHENA finite element code. The size of the finite element in ATHENA was chosen equal to one twelfth of the shortest wavelength, which is that of the shear waves (possible generation by mode conversion). For a frequency of 2.25 MHz we obtained a value of 0.1 mm.

Figure 14 shows the configuration tested: in immersion, in transmission mode, in normal incidence. The emitter is a single element (Ø12.7 mm). It is positioned at a distance of 20 mm from the face side and maintains a fixed position with respect to the axis of the weld during the simulation. The "receiving line" is positioned 4 mm from the opposite surface and extends over a length of 70 mm (from -35 mm to +35 mm). The listening line records the received signal at each mesh point, and an echodynamic curve is extracted, which corresponds to the maximal amplitude of the received signal at each point. In addition, Figure 14 again highlights the effects of beam deviation and splitting within the welds.

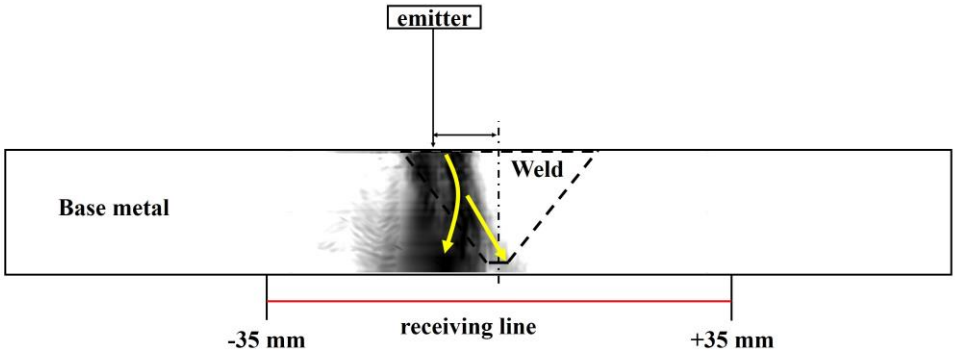

Figure 14: Configuration of ultrasonic simulations (transmitter position: -10 mm).

For the four weld mock-ups, we performed a total of eleven simulations through the macrostructures measured and predicted for eleven fixed positions of emitter in relation to the weld axis: -10, -8, -6, -4, -2, 0, +2, +4, +6, +8, +10 (data in millimetres). Figure 14 presents the simulated results for two fixed positions of the emitter (-10 and 0 mm with respect to the weld axis) in order to study the propagation of ultrasonic waves fairly close to the chamfer (-10 mm) and quite within the weld (0 mm, on the weld centreline). The blue curves are obtained by inputting the orientations measured on the macrographs, and the red curves those resulting from the model.

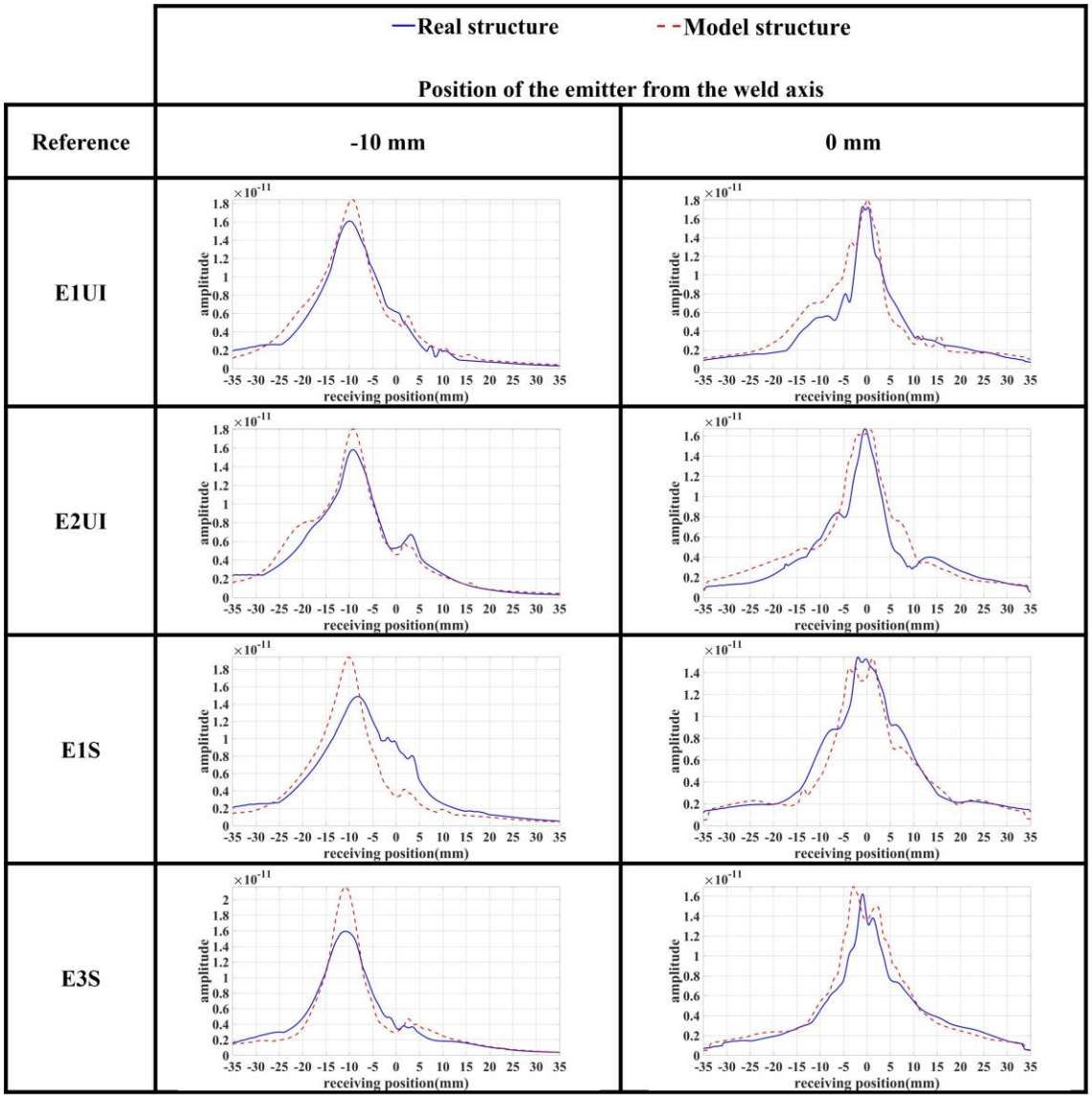

Figure 15: Comparison of simulated echodynamic curves from measured (real structure, in blue) and predicted (model structure, in red) grain directions.

These results show that for welds E1UI, E2UI and E3S, for the position of the emitter at -10 mm with respect to the axis of the weld, a good match is obtained for the ultrasonic propagation through the modelled structure compared to the propagation through the real one. The global shape of the transmitted beam is well recovered, thus deviations and splittings are properly modelled. The amplitude seems more sensitive to the modelling errors but the amplitude differences remain reasonable.

With regard to the simulated results obtained for an emitter position at 0 mm from the weld axis, it can be seen that for welds E1UI, E2UI and E3S, the results are again in good agreement. Despite global average modelling errors of between 14° and 20°, the effects of deviation and splitting of the ultrasonic beam are correctly predicted.

Concerning the E1S weld, higher discrepancies are observed which are caused by higher modelling errors within the welded area (see Figure 12 in section 4.1). The energy spread at -10mm in the case of the actual structure is not found in the case of the simulated structure. The beam was therefore not deflected in the same way. And at 0mm, a beam splitting between the x-axis -5mm and 5mm appears in the case of the modelled structure. Indeed, we are at the limit of the model's validity here. However, these differences obtained are not prohibitive and the model still provides a rather good description of ultrasonic propagation.

5. Conclusion

We have developed a new model adapted to GTAW welds. It is based among other things on the analysis of macrographs of cross sections of beads on plate. This makes it possible to avoid measuring phenomenological parameters (in particular remelting parameters) on weld macrographs, this measurement being complex. The model calculates the local thermal gradient at the pass scale and then takes into account the position of the pass in the chamfer. Finally, it reproduces the phenomena of selective and epitaxial growth to infer the orientation of the grains throughout the weld.

The macrostructure prediction of the developed model is in good agreement with the macrostructures of the mock-ups, with global average errors between 14° and 20°.

Ultrasonic simulations show that the resulting propagation through the modelled and the real macrostructures are also in good agreement. The welding model allows the deviations and splittings of the beam to be clearly reproduced and identified. However, in the case of the weld manufactured at very high welding speed, we observed larger differences in grain orientation between the model and the actual structure, resulting in equally larger differences in ultrasonic results. Thus, this is a model validity limit for high welding speeds.

In addition, it has been shown that the dimensions of a bead on plate change rather linearly with respect to welding power and speed, the other parameters having been set. It should therefore be possible to deduce the dimensions of a bead on plate in the long term by only knowing the welding power and speed.

The development of this model will continue along three main workstreams.

Firstly, concerning the order of passes, previous works for SMAW welds showed that this parameter had a dominant impact on the macrostructure. Currently, this parameter is integrated in the model but fixed at "American". We continue in this direction by manufacturing new mock-ups where the order of passes varies.

Secondly, we plan to perform other ultrasonic testing configuration, in oblique incidence, for example longitudinal waves at 60°, which will allow, on the one hand to use an industrial configuration, and on the other hand, to carry on the validation stage of this new model.

Thirdly, concerning the welding position, it will be necessary to integrate a 3D modelling of the macrostructure. Indeed, the 2D hypothesis is valid for the downhand welding position, but it is no longer valid for the other welding positions (vertical-up, horizontal-vertical and overhead), frequently used in industry.

Acknowledgements

This work was supported through the 'Generation IV / Sodium Fast Reactors / ASTRID' French program with CEA and LMA collaboration.
This work was developed within the framework of the MISTRAL joint research laboratory between LMA and CEA.
The authors thank the LTA of CEA Saclay for the manufacturing of the GTAW welds mock-ups.
The authors also thank EDF R&D for enabling them to use the ATHENA code for ultrasonic propagation modelling.

Bibliography

[1] K. Easterling, Introduction to the Physical Metallurgy of Welding, 2nd ed., Elsevier, 1992. https://doi.org/10.1016/C2013-0-04524-0.
[2] G. Corneloup, C. Gueudré, Non Destructive Testing and testability of materials and structures (Le contrôle non destructif et la contrôlabilité des matériaux et structures), Presses Polytechniques et Universitaires Romandes, 2017.
[3] B. Chassignole, R. El Guerjouma, M.A. PLOIX, T. Fouquet, Ultrasonic and structural characterization of anisotropic austenitic stainless steel welds: Towards a higher reliability in ultrasonic non-destructive testing, NDT E Int. 43 (2010) 273–282. https://doi.org/10.1016/j.ndteint.2009.12.005.
[4] J. Moysan, A. Apfel, G. Corneloup, B. Chassignole, Modelling the grain orientation of austenitic stainless steel multipass welds to improve ultrasonic assessment of structural integrity, Int. J. Press. Vessels Pip. 80 (2003) 77–85. https://doi.org/10.1016/S0308-0161(03)00024-3.
[5] J.A. Ogilvy, Computerized ultrasonic ray tracing in austenitic steel, NDT Int. 18 (1985) 67–77. https://doi.org/10.1016/0308-9126(85)90100-2.
[6] O. Nowers, D.. Duxbury, B.. Drinkwater, Ultrasonic array imaging through an anisotropic austenitic steel weld using an efficient ray-tracing algorithm, NDT E Int. 79 (2016) 98–108. https://doi.org/10.1016/j.ndteint.2015.12.009.
[7] H. Zhou, Z. Han, D. Du, Y. Chen, A combined marching and minimizing ray-tracing algorithm developed for ultrasonic array imaging of austenitic welds, NDT E Int. 95 (2018) 45–56. https://doi.org/10.1016/j.ndteint.2018.01.008.
[8] S.R. Kolkoori, M.U. Rahman, P.K. Chinta, M. Ktreutzbruck, M. Rethmeier, J. Prager, Ultrasonic field profile evaluation in acoustically inhomogeneous anisotropic materials using 2D ray tracing model: Numerical and experimental comparison, Ultrasonics. 53 (2013) 396–411. https://doi.org/10.1016/j.ultras.2012.07.006.
[9] N. Gengembre, A. Lhémery, Pencil method in elastodynamics: Application to ultrasonic field computation, Ultrasonics. 38 (2000) 495–499. https://doi.org/10.1016/S0041-624X(99)00068-2.
[10] A. Gardahaut, K. Jezzine, D. Cassereau, Paraxial ray-tracing approach for the simulation of ultrasonic inspection of welds, in: AIP Conf. Proc., 2014: pp. 529–536. https://doi.org/10.1063/1.4864865.
[11] A. Gardahaut, K. Jezzine, D. Cassereau, Modelling tools for ultrasonic inspection of bimetallic welds, in: ResearchGate, Nantes, France, 2012. https://www.researchgate.net/publication/272786660_Modelling_tools_for_ultrasonic_inspection_of_bimetallic_welds (accessed September 23, 2020).
[12] M. Darmon, N. Leymarie, S. Chatillon, S. Mahaut, Modelling of scattering of ultrasounds by flaws for NDT, in: A. Leger, M. Deschamps (Eds.), Ultrason. Wave Propag. Non Homog. Media, Springer, Berlin, Heidelberg, 2009: pp. 61–71. https://doi.org/10.1007/978-3-540-89105-5_6.
[13] E. Becache, P. Joly, C. Tsogka, An Analysis of New Mixed Finite Elements for the Approximation of Wave Propagation Problems, SIAM J. Numer. Anal. 37 (2000) 1053–1084. https://doi.org/10.1137/S0036142998345499.
[14] E. Becache, P. Joly, C. Tsogka, Fictitious domains, mixed finite elements and perfectly matched layers for 2-d elastic wave propagation, J Comput Acoust. 9 (2001) 1175–1201. https://doi.org/10.1142/S0218396X01000966.
[15] K.J. Langenberg, R. Hannemann, T. Kaczorowski, R. Marklein, B. Koehler, C. Schurig, F. Walte, Application of modeling techniques for ultrasonic austenitic weld inspection, NDT E Int. 33 (2000) 465–480. https://doi.org/10.1016/S0963-8695(00)00018-9.

[16] V. Schmitz, F. Walte, S.V. Chakhlov, 3D ray tracing in austenite materials, NDT E Int. 32 (1999) 201–213. https://doi.org/10.1016/S0963-8695(98)00047-4.
[17] M. Spies, Elastic waves in homogeneous and layered transversely isotropic media: Plane waves and Gaussian wave packets. A general approach, J. Acoust. Soc. Am. 95 (1994) 1748–1760. https://doi.org/10.1121/1.408694.
[18] B. Chassignole, D. Villard, M. Dubuget, J.-C. Baboux, R. el Guerjouma, Characterization of austenitic stainless steel welds for ultrasonic NDT, AIP Conf. Proc. 509 (2000) 1325–1332. https://doi.org/10.1063/1.1307835.
[19] S. Lu, H. Fujii, K. Nogi, Marangoni Convection and Gas Tungsten Arc Weld Shape Variations on Pure Iron Plates, Isij Int. - ISIJ INT. 46 (2006) 276–280. https://doi.org/10.2355/isijinternational.46.276.
[20] M. Tanaka, T. Shimizu, T. Terasaki, M. Ushio, F. Koshi-ishi, Y. C.-L, Effects of activating flux on arc phenomena in gas tungsten arc welding, Sci. Technol. Weld. Join. 5 (2000) 397–402. https://doi.org/10.1179/136217100101538461.
[21] M. Tanaka, J.J. Lowke, Predictions of weld pool profiles using plasma physics, J. Phys. Appl. Phys. 40 (2006) R1–R23. https://doi.org/10.1088/0022-3727/40/1/R01.
[22] K.. Mills, B.. Keene, Factors affecting variable weld penetration, Int. Mater. Rev. 35 (1990) 185–216. https://doi.org/10.1179/095066090790323966.
[23] S.. David, J.. Vitek, Correlation between solidification parameters and weld microstructures, Int. Mater. Rev. 34 (1989) 213–245. https://doi.org/10.1179/imr.1989.34.1.213.
[24] C.. Heiple, J.. Roper, R.. Stagner, R.. Aden, Surface-Active Element Effects on the Shape of Gta, Laser, and Electron-Beam Welds, Weld. J. 62 (1983) S72–S77.
[25] M.L. Lin, T.W. Eagar, Pressures produced by gas tungsten arcs, Metall. Trans. B. 17 (1986) 601–607. https://doi.org/10.1007/BF02670227.
[26] S. Kou, Welding Metallurgy, 2nd Edition, Wiley-Blackwell, Hoboken, N.J, 2002.
[27] A. Apfel, J. Moysan, G. Corneloup, M. Fouquet, B. Chassignole, Coupling an ultrasonic propagation code with a model of the heterogeneity of multipass welds to simulate ultrasonic testing, Ultrasonics. 43 (2005) 447–56. https://doi.org/10.1016/j.ultras.2004.09.004.
[28] C. Gueudré, L. Le Marrec, M. Chekroun, J. Moysan, B. Chassignole, G. Corneloup, Determination of the order of passes of an austenitic weld by optimization of an inversion process of ultrasound data, AIP Conf. Proc. 1335 (2011) 639–646. https://doi.org/10.1063/1.3591910.
[29] J. Moysan, S.. Song, H.. Kim, B. Chassignole, C. Gueudré, O. Dupond, Influence of welding passes on grain orientation – The example of a multi-pass V-weld, Int. J. Press. Vessels Pip. 93–94 (2012). https://doi.org/10.1016/j.ijpvp.2012.02.007.
[30] T. Lienert, T. Siewert, S. Babu, V. Acoff, eds., Fundamentals of Weld Solidification, in: Weld. Fundam. Process., ASM International, 2011: pp. 96–114. https://doi.org/10.31399/asm.hb.v06a.a0005609.